Electrochimica Acta 548 (2026) 147870

Contents lists available at ScienceDirect

Electrochimica Acta

journal homepage: www.journals.elsevier.com/electrochimica-acta

Comparative study of cobalt, copper and zinc oxides for the electrochemical reduction of nitrate to ammonia

Simone Lombardi [a,1], Tatiana Rodriguez-Flores [a,1], Gabriele Prina [a], Viviana Cigolotti [b], Nicola Lisi [b], Enrico Berretti [c], Mohsin Muhyuddin [a], Rosanna Viscardi [b], Roberto Nisticò [a,*], Carlo Santoro [a,*]

[a] Department of Materials Science, University of Milano-Bicocca, U5, Via Roberto Cozzi 55, Milano 20125, Italy
[b] Casaccia Research Center, ENEA, Department of Energy Technologies and Renewable Sources, Via Anguillarese 301, 00123, Santa Maria di Galeria, Rome, Italy
[c] Istituto di Chimica Dei Composti OrganoMetallici (ICCOM), Consiglio Nazionale Delle Ricerche (CNR), Via Madonna Del Piano 10, Sesto Fiorentino, Firenze 50019, Italy

ARTICLE INFO

Keywords:
Ammonia electro-production
Electrocatalysis
Transition metal oxides
Nitrate reduction reaction
Platinum group metal-free electrocatalysts

ABSTRACT

Electrochemical nitrate reduction (NO_3RR) is gaining attention as a sustainable route for ammonia synthesis, offering a greener alternative to the energy-intensive Haber–Bosch process. In this work, we present a systematic and direct comparison of three representative metal oxide electrocatalysts (ECs), named CuO, ZnO, and Co_3O_4. These materials were synthesized following a simple co-precipitation route in an alkaline environment. This synthesis approach ensures consistent preparation conditions, allowing a more reliable assessment of their intrinsic electrocatalytic behavior. Structural and morphological characterizations, including XRD, SEM, HR-TEM, STEM, EDX, XRF and XPS, confirmed the formation of phase-pure oxides with distinct nanostructures: fibrous, needle-like CuO, plate-like Co_3O_4, and cauliflower-like ZnO. Moreover, binary mixtures of these oxides were also investigated to explore potential synergistic effects. Co_3O_4 emerged as the most promising EC to form NH_4^+, achieving a Faradaic efficiency (FE) of 94.3 % and a yield rate of 149.5 μmol h^{-1} cm^{-2} at −0.8 V vs RHE. In contrast, ZnO exhibited the lowest activity for NO_3RR, with FE below 16 % and yield rates below 7 μmol h^{-1} cm^{-2} at −0.8 V vs RHE. Instead, CuO showed high selectivity towards the partial reduction of NO_3^- to NO_2^- (FE up to 79.6 % and yield rate of 586.9 μmol h^{-1} cm^{-2}), with limited NH_4^+ formation (FE 20.8 %, 40.8 μmol h^{-1} cm^{-2}). These findings highlight the potential of Co_3O_4 as an efficient platinum group metal-free (PGM-free) EC for selective and efficient ammonia production.

1. Introduction

The commodity chemical sector is among the major energy consumers and transitioning this sector to lower-carbon alternatives could significantly reduce global carbon dioxide emissions [1]. One promising approach to achieve this goal is the electrification of chemical processes, using renewable energy sources to reduce the carbon footprint of chemical production. In fact, even if the energy consumption itself is not inherently problematic, it is a clear indicator of undesirable greenhouse gas (GHGs) emissions, since chemicals with high energy consumption also tend to have significant GHG emissions [2].

In particular, during the production of these chemicals, significant sources of GHG emissions are the combustion of fossil fuels necessary to generate the process energy and the production of feedstocks. In the case of ammonia (NH_3), its production is typically based on the Haber-Bosch process (HBP), an energy-intensive method (>600 KJ mol^{-1}), which requires demanding conditions of high pressures and high temperatures (150–350 atm, 350–550 °C) [3]. As for the feedstock, H_2 is entirely produced through steam reforming natural gas, which consumes 3–5 % of the global natural gas supply and is responsible for approximately 450 million metric tons of CO_2 emissions annually [4]. Due to this, the HBP is responsible for almost 11 % of overall global industrial CO_2 emissions [5,6]. For these reasons, electrochemical systems are gaining growing attention as potential alternatives to this process. In particular, the electrochemical reduction of nitrogen (N_2) has become a major focus of research in the past decade [7]. In this scenario, NH_3 would be

* Corresponding authors.
E-mail addresses: roberto.nistico@unimib.it (R. Nisticò), carlo.santoro@unimib.it (C. Santoro).
[1] Both authors contributed equally to this work.

https://doi.org/10.1016/j.electacta.2025.147870
Received 25 September 2025; Received in revised form 11 November 2025; Accepted 22 November 2025
Available online 23 November 2025

synthesized directly from N_2 present in the atmosphere in a carbon-neutral manner by using water molecules as the proton and electron source, and supplying the required energy through renewable technologies such as solar or wind [8].

However, the high bond energy (941 kJ mol^{-1}) of the N≡N bond, the low solubility of N_2 in water, and the competitive hydrogen evolution reaction (HER) seriously hinder the development and application of the nitrogen reduction reaction (NRR) [9,10]. As an alternative, researchers have shifted their focus toward closing the nitrogen cycle by electrochemically reducing more oxidized and reactive nitrogen-containing species back into NH_3 [11–13]. Nitrates (NO_3^-) and nitrites (NO_2^-) are ions present in water bodies due to the over-fertilization adopted in agriculture [14] and they are considered poisonous for the environment and an indicator of low quality of the water. Concerning civil water treatment, nitrates and nitrites are present at high concentrations due to the decomposition of urea coming from human urine [15]. Stringent discharge limits impose the reduction of nitrite and nitrates in water bodies before discharge [16]. Other industrial activities and processes also produce wastewater rich in nitrates, such as explosives, food industries, fireworks, weapons, etc [17,18].

Due to the aqueous electrolyte being easier to handle, high solubility of NO_3^- in water and the low bond energy of the $N = O$ bond (204 kJ mol^{-1}) compared to the 941 kJ mol^{-1} of the N≡N bond, there is increasing interest in developing electrochemical NO_x reduction technologies driven by renewable electricity [14].

Furthermore, excessive nitrate levels in surface and groundwater can severely impact ecosystems by promoting eutrophication and pose serious risks to human health, including methemoglobinemia, nausea, elevated heart rate, and an increased risk of "blue baby syndrome" [19–23]. In this context, the nitrate reduction reaction (NO_3RR) approach offers a dual benefit: from one side, it enables the sustainable production of NH_3 under ambient conditions, and from the other side, it simultaneously removes harmful nitrates from the environment. Besides this, if electricity is provided through renewable energy sources (e.g., solar, wind), this process can be considered totally green and could contribute to electrifying, at least partially, an industrial sector such as NH_3 production, which is crucial for reaching the complete decarbonization goal set by the EU in 2050 [24].

The electrochemical conversion of NO_3^- to NH_3 involves the transfer of eight electrons and multiple reaction intermediates, as nitrogen exhibits a wide range of stable hydrides and oxides with valence states ranging from −3 to +5 [14]. Several mechanistic pathways have been proposed in the literature, highlighting the role of key adsorbed species such as NO_2*, NO*, and NH_2OH* in determining the reaction selectivity. To provide a general overview, the main intermediates and possible competing routes are summarized in Fig. 1, adapted from recent reports [25–27].

Hence, the development and investigation of efficient electrocatalytic platinum group metal-free (PGM-free) materials is crucial for improving both the activity of the electrocatalysts (ECs) and selectivity during NO_3RR towards the desired product.

Cu-based materials are considered highly promising NO_3RR ECs as Cu not only exhibits strong nitrate adsorption ability, but also promotes fast kinetics in the rate-determining step (RDS) involving the reduction of $*NO_3$ to $*NO_2$. This is attributed to its highly occupied d orbitals, which are energetically aligned with the π LUMO of NO_3^-, which facilitates an efficient electron transfer [27].

In our previous work, we examined several design strategies to enhance the electrochemical performance of copper-based materials for NO_3RR, and among them, the formation of heterojunctions was identified as a key parameter for improving the electrocatalytic behavior [28]. For instance, *Wang* et al. [29]. demonstrated that CuO nanowire arrays (NWAs) undergo an in situ electrochemical transformation into Cu/Cu_2O under cathodic potentials. Operando Raman spectroscopy, supported by complementary ex situ analyses, confirmed this structural reconstruction, indicating the formation of a Cu/Cu_2O heterostructure that serves as an active phase. Combined differential electrochemical mass spectrometry (DEMS) and density functional theory (DFT) calculations further revealed that interfacial electron transfer from Cu_2O to Cu facilitates the formation of *NOH intermediate, inhibiting the competing HER, thereby enhancing NO_3RR selectivity.

Similarly, *Xu* et al. [30]. designed core–shell Cu@$Cu_{2+1}O$ nanowires, where the conductive Cu core ensures efficient charge transport, and the $Cu_{2+1}O$ shell provides abundant catalytically active sites. Moreover, the electronic interaction at this interface shifts the Cu d-band center, tuning the adsorption energies of key intermediates.

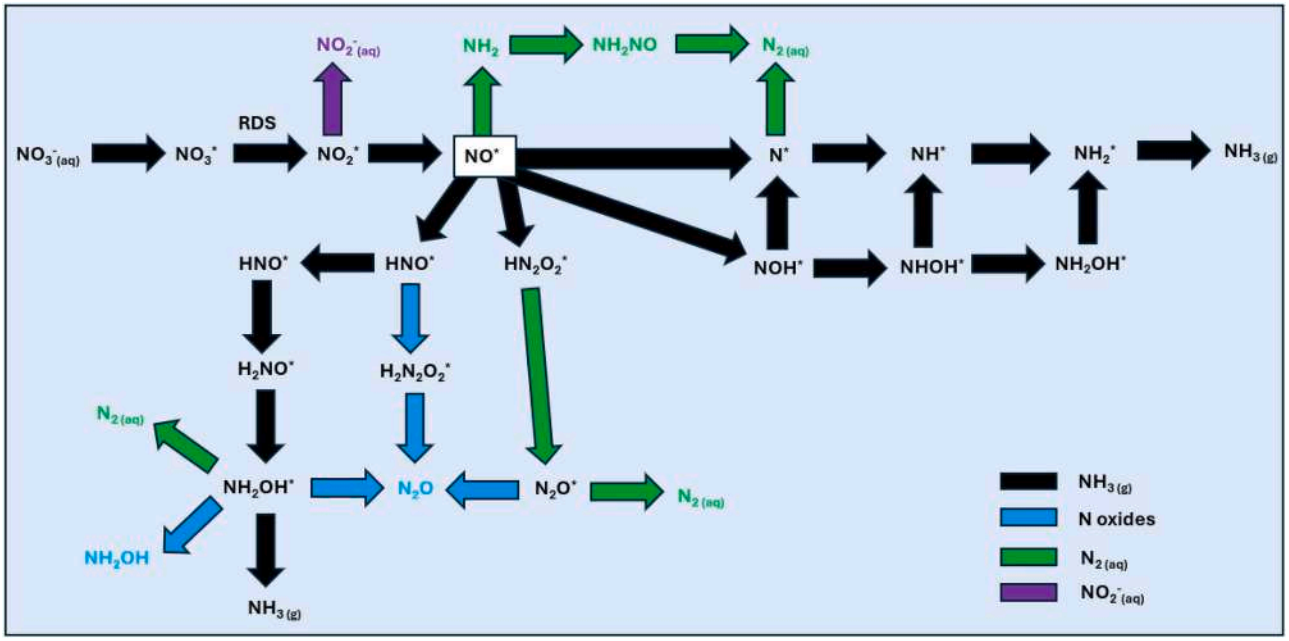

Fig. 1. Simplified reaction mechanism for NO_3RR. The scheme illustrates the main adsorbed intermediates (*) and the multiple competing pathways leading to different products. Black arrows represent the reduction pathways towards NH_3, while colored arrows highlight alternative routes for NO_2^- (purple), N oxides (light blue), and N_2 (green).

Co-based materials applied in NO_3RR registered a rapid progress since 2019 [31] driven by their low reaction barriers and high electrocatalytic activity [32–39]. Among the different Co-based ECs, Co_3O_4, which is a mixed-valence spinel structure containing both Co^{2+} and Co^{3+} species, showed promising activity and selectivity [29,40–43]. This material is particularly interesting because, despite its high performance, the origin of its activity remains debated, with ongoing discussion on whether tetrahedral Co^{2+} or octahedral Co^{3+} sites play the dominant role in driving NO_3RR.

Recently, Sun et al. [44]. conducted an interesting study, performing DFT calculations to determine the free energy of each of these intermediates on the octahedral Co^{3+}species in the (110) plane and the tetrahedral Co^{2+}species in the (111) plane. The results revealed that on the Co_3O_4 (111) plane, the RDS is the desorption of $*NH_3$ with a Gibbs free energy change of 0.73 eV. In contrast, on the Co_3O_4 (110) plane, the RDS is the conversion of *NO to *N, requiring a much higher energy input of 1.27 eV. Furthermore, the calculated adsorption energy (E_{ads}) of $*NO_3$ on Co^{2+} sites of the (111) plane is −3.37 eV, significantly lower than that on Co^{3+} sites of the (110) plane (−2.15 eV), indicating a stronger interaction and adsorption preference on the Co^{2+}-rich (111) surface.

The charge accumulations and depletion on the two sites, where an increased electron deficiency on Co sites reflects a stronger electron donation to nitrate's oxygen atoms, enhancing the deoxygenation process [45]. These findings suggest that the NO_3RR primarily occurs on Co^{2+} sites exposed on the (111) facets. Additionally, the adsorption energies of *H were calculated to be 1.92 eV and 0.68 eV for the (110) and (111) planes, respectively, both higher than those of $*NO_3$, indicating that NO_3RR is more favorable than HER on both surfaces.

Lastly, regarding Zn-based materials, even if ZnO is a relatively low-cost material, with intrinsic advantages, including non-toxicity, high stability [46] and tunable electronics [47], only a few studies are available in the literature reporting its performance during NO_3RR [48–50]

In this work, three representative transition-metal oxides (CuO, ZnO, and Co_3O_4) were selected based on their distinct electronic structures and catalytic behaviors toward NO_3RR. All materials were synthesized through a simple alkaline co-precipitation route performed under soft conditions (short reaction time, no organic solvents or high-temperature calcination), ensuring uniform and reproducible preparation parameters. This mild synthesis strategy allows a direct comparison of the intrinsic electrocatalytic activity of each oxide, independent of the influence of dopants, supports, complex growth environments, or oxygen-vacancy engineering. Furthermore, binary mixtures of these oxides were also prepared and evaluated electrochemically to explore potential synergistic effects towards NO_3RR.

2. Experimental

2.1. Chemicals

Reactants: copper(II) nitrate trihydrate ($Cu(NO_3)_2{\bullet}3H_2O$, 99 %, CAS 10,031–43–3, Thermo Scientific), zinc(II) nitrate hexahydrate ($Zn(NO_3)_2{\bullet}6H_2O$, 98 %, CAS 10,196–18–6, Alfa Aesar), cobalt(II) nitrate hexahydrate ($Co(NO_3)_2{\bullet}6H_2O$, 99 %, CAS 10,026–22–9, Sigma-Aldrich), and sodium hydroxide pellets (NaOH, ACS reagent, ≥98 %, CAS 1310–73–2, Sigma-Aldrich). Solutions and solvents: deionized water was used during washing procedures. Milli-Q water with a resistivity of 18.2 MΩ cm was used. All chemicals were used without further purification.

2.2. Synthesis

The metal oxides (CuO, ZnO, and Co_3O_4) were synthesized following a co-precipitation method. Initially, an aqueous solution of the corresponding transition metal nitrate salt ($TM(NO_3)_2{\cdot}nH_2O$) was prepared by dissolving the precursor in 50 mL of deionized water under constant stirring at room temperature (RT) for 10 min. The resulting solution was then transferred to a 250 mL two-necked flask, supplemented with an additional 50 mL of deionized water, and heated up to 90 °C under continuous stirring. Once the target temperature was reached, 20 mL of a 2 M NaOH solution was added dropwise over a period of 10 min. The reaction mixture was maintained at 90 °C with constant stirring for 30 min to allow complete precipitation and the formation of the metal hydroxides. Afterward, the mixture was allowed to naturally cool down to RT and subjected to centrifugation at 9000 rpm for 10 min. The resulting precipitate was washed three times with deionized water and once with ethanol to remove residual ions and byproducts. Finally, washed precipitates were dried overnight in an air oven at 75 °C and then ground into a fine powder using an agate mortar. A heat treatment was then applied, namely: (i) heating ramp from RT to 450 °C (10 °C/min), followed by (ii) isothermal step at 450 °C for 4 h, and (iii) a cooling ramp from 450 °C to 50 °C (5 °C/min).

Regarding the binary mixtures of oxides (i.e., CuO–ZnO, CuO–Co_3O_4, ZnO–Co_3O_4), equimolar amounts of the two metal oxide powders (50:50 wt %) were thoroughly homogenized using a mortar and pestle for at least 30 min to ensure uniform mixing.

2.3. Characterizations

X-Ray diffraction (XRD) analysis was carried out using a Rigaku Miniflex 600 diffractometer equipped with a copper anode (operated at 40 kV and 15 mA). Diffraction patterns were collected within the 2θ range of 20° to 80°, employing a scan step of 0.02° and a scanning speed of 1.0° per minute. Phase identification was conducted by matching the experimental patterns with standard reference data from the ICDD database, using the PDXL-2 software suite. This software also facilitated the refinement and determination of lattice parameters. Furthermore, the average crystallite size (t) was estimated using the Scherrer equation Eq. (2):

$$\tau = \frac{k\lambda}{FWHM(\cos\theta)} \quad (2)$$

The shape factor (k) was taken as 0.9, the X-ray wavelength (λ) was 0.154 nm (Cu Kα radiation), FWHM is the full width at half maximum of the main diffraction peak (corrected for instrumental broadening and expressed in radians), and the angle θ refers to the Bragg angle (expressed in radians). In the case of the different ECs, the following diffraction peaks were considered, namely 38.7° 2θ for CuO (corresponding to the Miller index (111)), 36.2° 2θ for ZnO (corresponding to the Miller index (101)), and 36.9° 2θ for Co_3O_4 (corresponding to the Miller index (311)). Lattice constants were determined through analysis performed with the instrumental PDXL-2 software.

The morphological and microstructural properties of the samples were examined using scanning electron microscopy (SEM) on a Zeiss Gemini 500 microscope, which features a field emission gun (FEG) and is equipped with a Bruker Quantax EDS system for elemental composition analysis. Imaging was performed at an accelerating voltage of 5.0 kV, utilizing the in-lens detector to obtain high-resolution surface images. Before SEM observation, powdered specimens were placed onto a metallic sample holder using conductive carbon tape and then coated with a thin gold layer via sputter coating by means of a VPI SD-900C device to prevent charging artifacts. Particle dimensions were measured by analyzing 100 particles using ImageJ software for particle size distribution assessment. High-resolution transmission electron microscopy (HR-TEM), scanning transmission electron microscopy (STEM) and energy-dispersive X-ray spectroscopy (EDX) analyses were carried out using a Thermo Fisher Talos F200X G2 microscope operating at an accelerating voltage of 200 kV. The EDX maps were taken with a Super X spectrometer equipped with four 30 mm^2 silicon drift detectors with a collection angle of 0.7 srad. Data processing and arrangement have been performed with the Thermofisher proprietary software VELOX.

X-ray fluorescence (XRF), having an X-ray tube with a molybdenum anode (Bruker Artax 200 spectrometer), was utilized to perform qualitative elemental analysis.

The powder samples were analyzed with X-ray photoelectron spectroscopy (XPS) Escalab Qxi (Thermofisher), and the core spectra acquired using a monochromatic Al source (1486.6 eV) and standard charge neutralization. Samples were placed in three separate slots of the power sample holder.

2.4. Preparation of the working electrode

The electrocatalyst ink was prepared by dispersing 5 mg of EC powder in a solution containing 670 μL of isopropanol (IPA), 300 μL of Milli-Q water, and 30 μL of a 5 wt % Nafion solution. The suspension was sonicated in an ultrasonic bath for 15 min, followed by probe sonication for 1 h using a pulsed mode (5 s on / 5 s off) at 30 % amplitude. For linear sweep voltammetry (LSV) measurements, 19.6 μL of the EC ink was drop-cast onto a glassy carbon electrode (geometric area: 0.1962 cm^2), resulting in an EC loading of 0.5 mg cm^{-2}.

For chronoamperometry (CA) experiments, a TGP-H-60 carbon paper (thickness: 0.20 ± 0.05 mm) was used as received, without any pre-treatment. A volume of 100 μL of EC ink was drop-cast on the carbon paper with a 1 cm^2 geometric working area for an EC loading of 0.5 mg cm^{-2} (**Fig. S1a**).

2.5. Linear sweep voltammetry

To evaluate both the HER and NO_3RR activity, LSVs were performed. All measurements were carried out using a Biologic potentiostat in a single-compartment electrochemical cell equipped with a rotating disk electrode (RDE). A glassy carbon electrode (geometric area: 0.1962 cm^2) was employed as the working electrode, with a graphite rod as the counter electrode and a reversible hydrogen electrode (RHE) as the reference. HER activity was measured in a 0.1 M phosphate buffer solution (PBS) composed of 0.074 M KH_2PO_4 and 0.026 M K_2HPO_4. For NO_3^-RR measurements, the electrolyte consisted of 0.1 M PBS with an additional 0.16 M NO_3^- (KNO_3). Prior to LSV, cyclic voltammetry was performed in the potential range from 0 V to −1 V vs RHE, at a scan rate of 50 mV s^{-1} and a rotation speed of 1600 rpm, until stable polarization curves were obtained. Subsequently, LSV was conducted (0 V to −1 V, 20 mV s^{-1}, 1600 rpm), and repeated three times. The reported curves represent the average of these three measurements. Note that the applied potentials for all electrochemical tests were iR corrected.

2.6. Chronoamperometry

Electrochemical nitrate reduction measurements were carried out in a two-compartment H-type cell (**Fig. S1b**), separated by an Aquivion® E87–12 S proton exchange membrane (PEM) used as received without pre-treatment.

All measurements were conducted using a Biologic potentiostat. A standard three-electrode system was used with a reversible hydrogen electrode (HydroFlex®) and a graphite rod as the reference and counter electrode, respectively. The electrolyte used for all nitrate reduction experiments is a 0.1 M PBS with an additional 0.16 M, 0.12 M, 0.08 M or 0.04 M NO_3^-(KNO_3). Both the working and counter chambers were filled with 30 mL of electrolyte. The pH of the electrolyte was set to 6.3 to ensure that the produced ammonium (NH_4^+) remains in its protonated form and does not convert to gaseous NH_3, considering the pKa of NH_4^+ (pKa: 9.24). This condition allows for accurate quantification of NH_4^+ via ion chromatography (IC). Both the counter and the working chambers contain 30 mL of the electrolyte. Chronoamperometric (CA) tests were performed for 1 h under constant magnetic stirring (200 rpm), at three different applied potentials: −0.40 V, −0.60 V, and −0.80 V vs. RHE.

2.7. Detection and determination of ammonium and nitrite ions

After each electrolysis experiment, the electrolyte from the working chamber was sampled and analyzed for NH_4^+ and NO_2^- concentrations by IC. Specifically, for the determination of ammonium, 1 mL of the electrolyte was transferred into a vial and diluted to a final volume of 10 mL (1:10 dilution). For nitrite analysis, 200 μL of electrolyte was diluted to 10 mL (1:50 dilution). Chromatographic separation was performed using a Metrohm Eco IC Ion Chromatograph system (Metrohm AG, Herisau, CH), equipped with a conductivity detector, a MSM conductivity suppressor and a Metrohm 863 Compact Autosampler. The IC was equipped with a Metrohm Metrosep A Supp 5 (4 mm × 250 mm) and a Metrosep A Supp 1 Guard/4.6 guard-column for anion separation and with a Metrosep C 6 (4 mm × 250 mm) and a Metrosep C 6 S-guard/4.0 guard-column for cations separation (Metrohm AG, Herisau, CH). For cation analysis, the mobile phase was a 4 mmol/L HNO_3 + 0.7 mmol/L oxalic acid aqueous solution, at a flow rate of 0.9 mL/min, at room temperature (25 °C). For anion analysis, the mobile phase was a 3.2 mmol/L Na_2CO_3 + 1.0 mmol/L $NaHCO_3$ aqueous solution, at a flow rate of 0.8 mL/min, at room temperature (25 °C). The injection volume was 10 μL. The eluent conductivity background was suppressed by using a Metrohm MSM cation-exchange membrane set in-line after the anionic column (no suppression was used for cations detection). It was regenerated with 100 mmol/L of sulfuric acid flowing countercurrently at a flow rate of 1.5 mL/min.

2.8. Calculation of the yield and faradic efficiency

For the nitrate reduction reaction (NO_3RR), the yield rate of ammonium (NH_4^+) was calculated using Eq. (3.1), while the corresponding Faradaic Efficiency (FE) was determined using Eq. (3.2):

$$\text{Yield rate } NH_4^+ = \frac{C\ NH_4^+ \cdot V}{MM\ NH_4^+ \cdot t \cdot S} \tag{3.1}$$

$$\text{FE } NH_4^+ = \frac{n \cdot F \cdot C\ NH_4^+ \cdot V}{MM\ NH_4^+ \cdot Q} \tag{3.2}$$

Similarly, for the partial reduction of nitrate to nitrite (NO_2^-), the yield rate and Faradaic Efficiency were calculated using Eq. (3.3) and Eq. (3.4), respectively:

$$\text{Yield rate } NO_2^- = \frac{C\ NO_2^- \cdot V}{MM\ NO_2^- \cdot t \cdot S} \tag{3.3}$$

$$\text{FE } NO_2^- = \frac{n \cdot F \cdot C\ NO_2^- \cdot V}{MM\ NO_2^- \cdot Q} \tag{3.4}$$

Where, C NH_4^+ and C NO_2^- are the mass concentrations (mg L^{-1}) of ammonium and nitrite, respectively; V is the volume of the electrolyte in the working chamber; t is the duration of the chronoamperometric experiment (1 h); S is the surface area of the working electrode (1 cm^2); n is the number of electrons transferred, for NO_3^- to NO_2^- is equal to 2, whereas for NO_3^- to NH_4^+ is equal to 8; MM NH_4^+ and MM NO_2^- are the molar masses of ammonium (18.04 g/mol) and nitrite (46.00 g/mol), respectively; F is the Faraday's constant (96.485 $Cmol^{-1}$), and Q is the total charge passed during electrolysis, calculated by integrating the current over time during chronoamperometry. Note that all error bars reported in this work represent the standard deviation from triplicate measurements performed using independently prepared electrodes.

3. Results and discussion

3.1. Morphological, structural, and surface properties

A comprehensive characterization of the synthesized metal oxides (CuO, ZnO, and Co_3O_4) was carried out using XRD, SEM, TEM, STEM-EDX, XRF, and XPS analyses to gain insight into their structural,

morphological, and chemical properties. The results are presented in the following order, moving from bulk crystal structure to morphology and elemental composition, down to surface chemical states.

The crystallographic characterization of the CuO, ZnO, and Co_3O_4 samples is shown in Fig. 2. The XRD analysis revealed the characteristic diffraction peaks corresponding to each oxide's typical crystal structure. For the CuO sample, the XRD pattern exhibits the main reflections at 2θ = 32.5° (110), 35.6° ($\bar{1}11$), 38.8° (111), 48.7° ($\bar{2}02$), 53.5° (020), 58.4° (202), 61.6° ($\bar{1}13$), 66.2° ($\bar{3}11$), 68.2° (220), 72.4° (311) and 75.1° ($\bar{2}22$) consistent with the monoclinic tenorite CuO phase (card number 01–080–1916, ICDD). For the Co_3O_4 sample, the XRD pattern shows the key peaks at 2θ = 19° (111)

31.3° (220), 36.8° (311), 38.5° (222), 44.8° (400), 55.6° (422), 59.3° (511), 65.2° (440), 69.7° (531) and 77.3° (533) which are typical of the cubic spinel Co_3O_4 structure (card number 01–080–1545, ICDD). For the ZnO sample, the XRD pattern exhibits prominent diffraction peaks at 2θ = 31.8° (100), 34.4° (002), 36.3° (101), 47.5° (102), 56.6° (110), 62.9° (103), 66.4° (200), 68.0° (112), 69.10° (201), 72.56° (004), and 76.95° (202) characteristic of the hexagonal wurtzite ZnO phase (card number 00–036–1451, ICDD). The comparative analysis of ZnO, CuO, and Co_3O_4 reveals significant differences in both crystallite size and lattice parameters, reflecting the distinct structural nature of each sample (see Table 1). The average crystallite size was calculated from the FWHM values using the Scherrer equation, which shows that CuO exhibits the smallest average crystallite size (10 nm), followed by Co_3O_4 (22 nm) and ZnO (29 nm). Regarding the lattice parameters, CuO presents a monoclinic lattice with three different cell parameters ($a = 4.69$ Å; $b = 3.42$ Å; $c = 5.13$ Å), ZnO exhibits a hexagonal wurtzite-type structure with two lattice parameters equal ($a = b = 3.25$ Å) and c parameter different ($c = 5.21$ Å), whereas Co_3O_4 displays a cubic symmetry with all lattice parameters equal to each other ($a = b = c = 8.08$ Å), which is characteristic for a spinel structure.

From the morphological viewpoint, SEM analysis was employed to

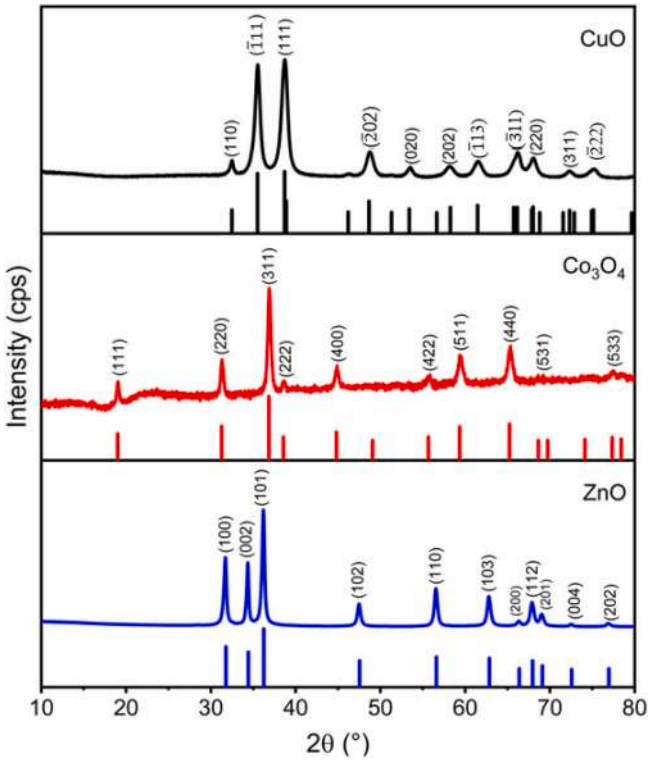

Fig. 2. XRD patterns of the synthesized samples: CuO (top, black), Co_3O_4 (middle, red), and ZnO (bottom, blue). Reference patterns: CuO (01–080–5897, black), Co_3O_4 (00–043–1003, red), and ZnO (00–036–1451, blue).

Table 1
Average crystallite sizes estimated using the Debye–Scherrer Equation, and lattice parameters obtained from instrumental software and for CuO, Co_3O_4, and ZnO samples.

Samples	Average crystallite size (nm)	Lattice parameter a (Å)	Lattice parameter b (Å)	Lattice parameter c (Å)
CuO	10	4.69	3.42	5.13
Co_3O_4	22	8.08	8.08	8.08
ZnO	29	3.25	3.25	5.21

investigate the particles' morphology and size distribution of the synthesized metal oxides. In particular, the CuO (Fig. 3**a** and 3**b**) sample exhibits a fibrous, needle-like (acicular) morphology, forming entangled and compact aggregates. High magnification images highlight surface roughness and sharp edges typical of these elongated structures. The mean particle length and width are 214.42 ± 94.03 nm and 49.28 ± 20.39 nm, respectively, with a coefficient of variation (CV) of 0.44 and 0.41, indicating considerable size variability (**Fig. S2**). In the case of Co_3O_4 (Fig. 3**c** and 3**d**) sample, instead, it exhibits a plate-like morphology, with rounded edges and is homogeneously distributed. At high magnification, the surface texture appears rough, with pronounced agglomerates and interparticle voids. Particle size analysis reveals a mean length of 203.50 ± 84.82 nm and a mean width of 135.84 ± 56.11 nm, with a CV of 0.42 and 0.41, respectively (**Fig. S3**). Finally, ZnO (Fig. 3**e** and 3**f**) displays a cauliflower-like morphology, with spherical agglomerated particles exhibiting a high morphological homogeneity. At high magnifications, it is possible to appreciate a granular texture. The particle size distribution ranges broadly from 200 to 800 nm, with a mean length of 575.72 ± 225.16 nm and a mean width of 473.48 ± 205.78 nm, with CVs of 0.39 and 0.43, respectively (**Fig. S4**).

The morphology, crystal structure, and elemental distribution of the synthesized metal oxides were further investigated by HR-TEM and STEM (Fig. 4) coupled with EDX (Fig. 5).

In particular, the bright-field STEM images confirmed the SEM analysis, with CuO particles showing a needle-like morphology (Fig. 4**a** and 4**b**), Co_3O_4 a plate-like morphology (Fig. 4**d** and 4**e**), and ZnO showing a cauliflower-like shape (Fig. 4***g*** and 4**h**). HR-TEM revealed well-defined lattice fringes for all samples, consistent with the crystalline phases identified by XRD. Specifically, for CuO (Fig. 4**c**), the main observed reflections were indexed to monoclinic CuO ([111] , 232 Å, 100 %), with minor contributions from additional CuO orientations (252 Å, [$\bar{1}$11] , 76 %), whereas other Cu-based oxides (Cu, Cu_2O and Cu_4O_3) were checked but not detected. For Co_3O_4 (Fig. 4**f**), the dominant reflections were assigned to the spinel phase ([311] , 2.43 Å, 100 %), with additional contributions from ([440] , 1.42 Å, 42 %) and ([400] , 2.85 Å, 30 %) orientations, whereas other Co-based phases (Co, CoO_2) were checked but not detected, confirming the exclusive presence of mixed-valence Co(II)/Co(III) of Co_3O_4. For ZnO (Fig. 4**i**), the observed lattice fringes were mainly indexed to the hexagonal wurtzite ZnO phase ([100] , 2.81 Å, 100 %), with additional contributions from ([110] , 1.62 Å, 66 %). Other Zn-based phases (hexagonal Zn metal, cubic ZnO) were checked, but their reflections were either overlapped or not clearly detected, with the best fit corresponding to the hexagonal ZnO structure.

These HR-TEM observations highlight the high crystallinity of the synthesized nanostructures at the local scale, with no detectable amorphous domains.

Elemental mapping by EDX in Fig. 5 confirmed a uniform distribution of oxygen and the corresponding metal elements throughout all samples, with no indications of significant phase segregation. No additional elements were detected apart from trace impurities (<3 %). XRF spectra are reported in **Fig. S5,** showing the presence of the specific transition metal used during the synthesis.

Finally, the surface chemical composition and oxidation states of the synthesized metal oxides were investigated by XPS. (**Fig. S6**)

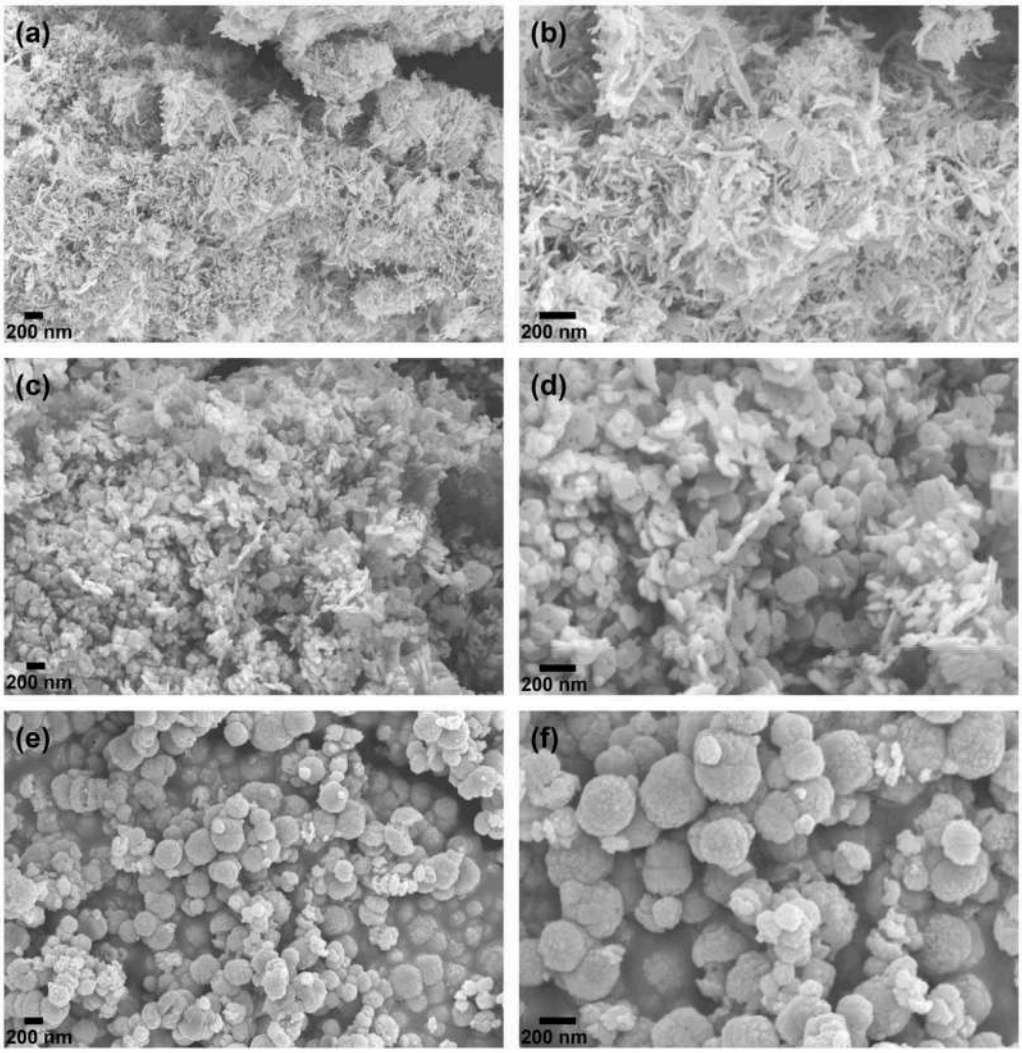

Fig. 3. SEM micrographs of (a,b) CuO, (c,d) Co_3O_4, and (e,f) ZnO samples at low (50 KX, left) and high (100 KX, right) magnifications.

The XPS analysis of the samples reveals that the three oxides have been produced in pure form without nitrogen (N1s at 400 eV) residues and with very limited carbon contamination (C1s at 285 eV), which might be due to the exposure to the environment of the powders before analysis (as seen in **Fig. S6a**).

The nature of the surface oxide is appreciated by further analysis of the 2p core level spectra of the metals Cu (**Fig. S6b**), Co (**Fig. S6c**) and Zn (**Fig. S6d**), respectively, at 933 eV, 779.7 eV and 1022 eV. It can be appreciated by the direct comparison with the literature [51,52] that the three oxide powders have a surface composition that confirms the XRD analysis, and are in the form, respectively, of CuO, Co_3O_4 and ZnO.

These results validate the chemical nature of the three oxides and provide additional insight into their surface composition, complementing the bulk structural and morphological characterization. The electrochemical performance of the individual oxides and their binary mixtures was subsequently investigated to assess their electrocatalytic activity toward NO_3RR.

3.2. Electrochemical performance

As a fundamental study, this work focused on neutral pH (pH 6.3) to evaluate the intrinsic activities of the different active sites in the developed metal oxides toward the NO_3RR.

For each EC, LSVs were recorded both in 0.1 M PBS and in 0.1 M PBS + 0.16 M NO_3^- to have a first evaluation of HER and NO_3RR activity, respectively.

The onset potential was defined as the potential at which the current density reached −0.4 mA cm^{-2}, enabling consistent comparison across materials [53]. Fig. 6**b** provides a visual comparison of the LSVs near the onset region and highlights the current threshold adopted in this study. The corresponding potential values at −0.4 mA cm^{-2} extracted from these LSVs are summarized in Fig. 6**c**.

As shown in Fig. 6**a**, CuO exhibited a strong electrocatalytic response in the presence of nitrate, with current densities exceeding −10 mA cm^{-2} at −1.0 V. In contrast, the current density in PBS alone remained below −1.5 mA cm^{-2}. This significant difference confirms a high specificity for NO_3^-RR and minimal HER interference. These observations are further supported by the low onset potential measured for CuO (−0.266 ± 0.007 V vs. RHE). Complete LSV profiles for all tested electrocatalysts are available in **Fig. S7** and **S8** and serve as the basis for the comparative analysis discussed below.

Co_3O_4 exhibited a relatively early onset (−0.442 ± 0.010 V vs. RHE), but the separation between the PBS and nitrate-containing curves was less pronounced. The CuO–Co_3O_4 binary mixture showed behavior like CuO, with the NO_3^-RR curve diverging from the PBS background at around −0.2 V vs. RHE and reaching approximately −9 mA cm^{-2}. The corresponding onset potential (−0.393 ± 0.007 V vs RHE) lies between those of CuO and Co_3O_4.

In contrast, ZnO displayed the least favorable activity, with nearly overlapping responses in both electrolytes and a delayed onset potential

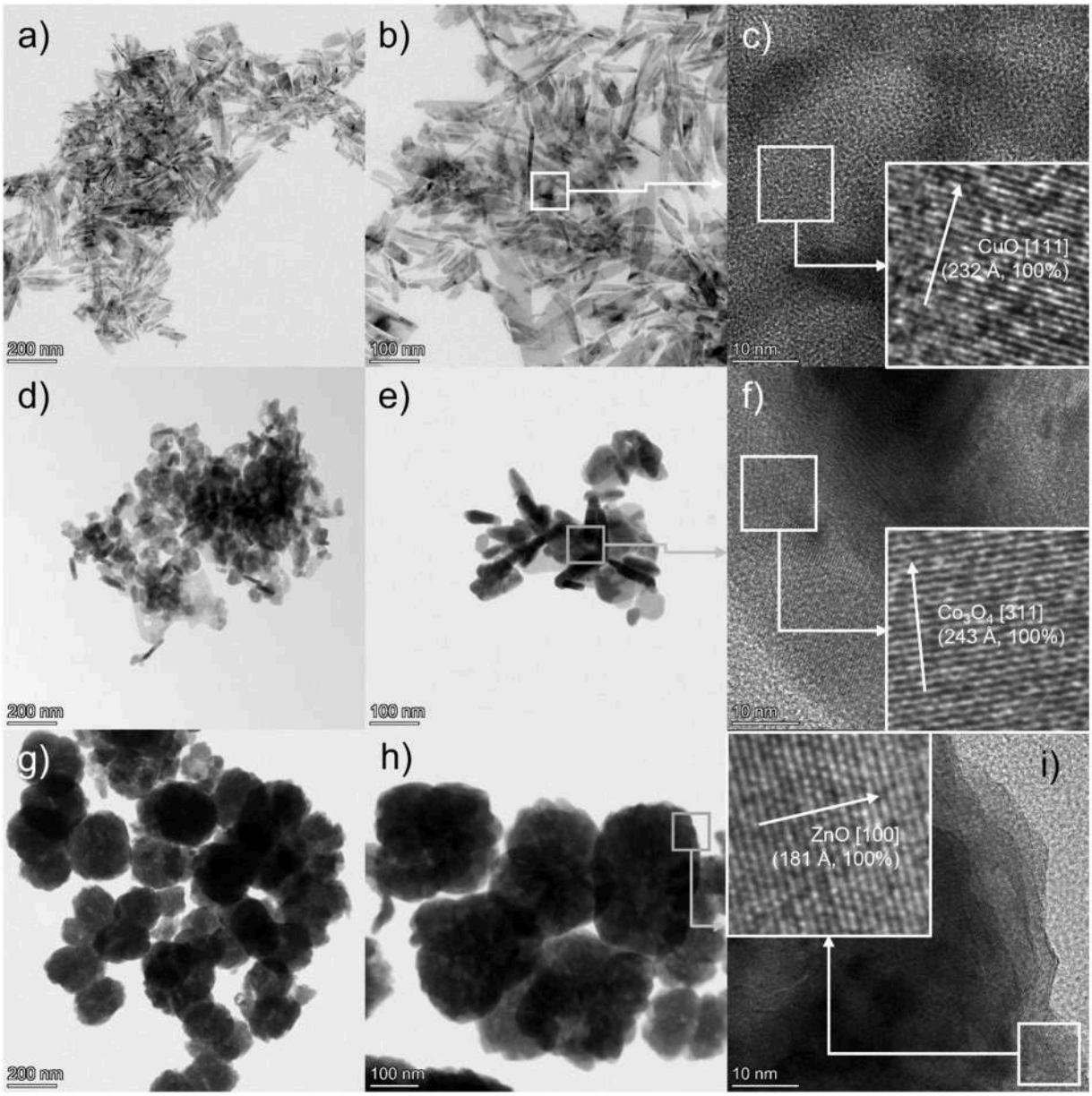

Fig. 4. STEM bright-field images (left, middle) and HR-TEM (right) of (a-c) CuO, (d-f) Co_3O_4, and (g-i) ZnO nanoparticles. The first two columns show the corresponding STEM bright-field images acquired at 70k x (left) and 130k x (middle). HR-TEM images are shown in the last column (right), taken at 1 MX magnifications.

(−0.736 ± 0.012 V vs RHE), pointing to poor activity toward NO_3RR and more favorable for HER.

ZnO–Co_3O_4 binary mixture showed very similar behavior to pure ZnO, with an onset potential of −0.755 ± 0.001 V and low current density in both conditions, suggesting that the electrochemical behavior is still dominated by the ZnO phase. Finally, ZnO–CuO binary mixture exhibited modest improvements over pure ZnO, with a slightly earlier onset potential (−0.625 ± 0.021 V vs RHE) and higher currents in the nitrate-containing solution.

To investigate the NO_3RR activity and selectivity of the different materials towards NH_4^+ and NO_2^-, a series of 1-h potential holds (chronoamperometry) were performed at−0.40 V, −0.60 V, and −0.80 V vs. RHE in 0.1 M PBS + 0.16 M NO_3^- (Fig. 7). The corresponding current–time profiles for each electrocatalyst are shown in **Fig. S9-S10.**

First, to establish the background activity of the substrate, chronoamperometry (CA) tests were conducted using bare carbon paper, without any electrocatalyst deposition.

The corresponding current–time profiles are shown in **Fig. S11a**. In all cases, a stable cathodic current was observed throughout the 1-hour test, with higher current densities at more negative potentials. During these experiments, significant bubble formation was visually detected on the electrode surface, strongly suggesting that the observed current arises predominantly from the evolution of hydrogen (HER) (**Fig. S11b**)

IC analysis of the electrolyte after these 1-h test revealed negligible amounts of NO_2^- and NH_4^+, confirming the absence of any substantial nitrate reduction on bare carbon paper. As a result, carbon paper is considered electrochemically inert toward NO_3RR under the tested conditions, and its contribution to the formation of reduction products will be neglected in the subsequent electrocatalytic evaluations.

At all applied potentials, CuO exhibited low selectivity toward NH_4^+ formation, with FEs of 5.4 % and 7.5 % at −0.4 V and −0.6 V, respectively, increasing to 20.8 % at −0.8 V (Fig. 7**a**). In contrast, CuO showed a remarkably high selectivity toward NO_2^-, with FEs remaining relatively stable across the tested potentials, 67.9 % at −0.4 V, 71.0 % at −0.6 V, and 79.6 % at −0.8 V, indicating only a slight increase with increasing overpotential. (Fig. 7**b**) The corresponding NO_2^- yield rates

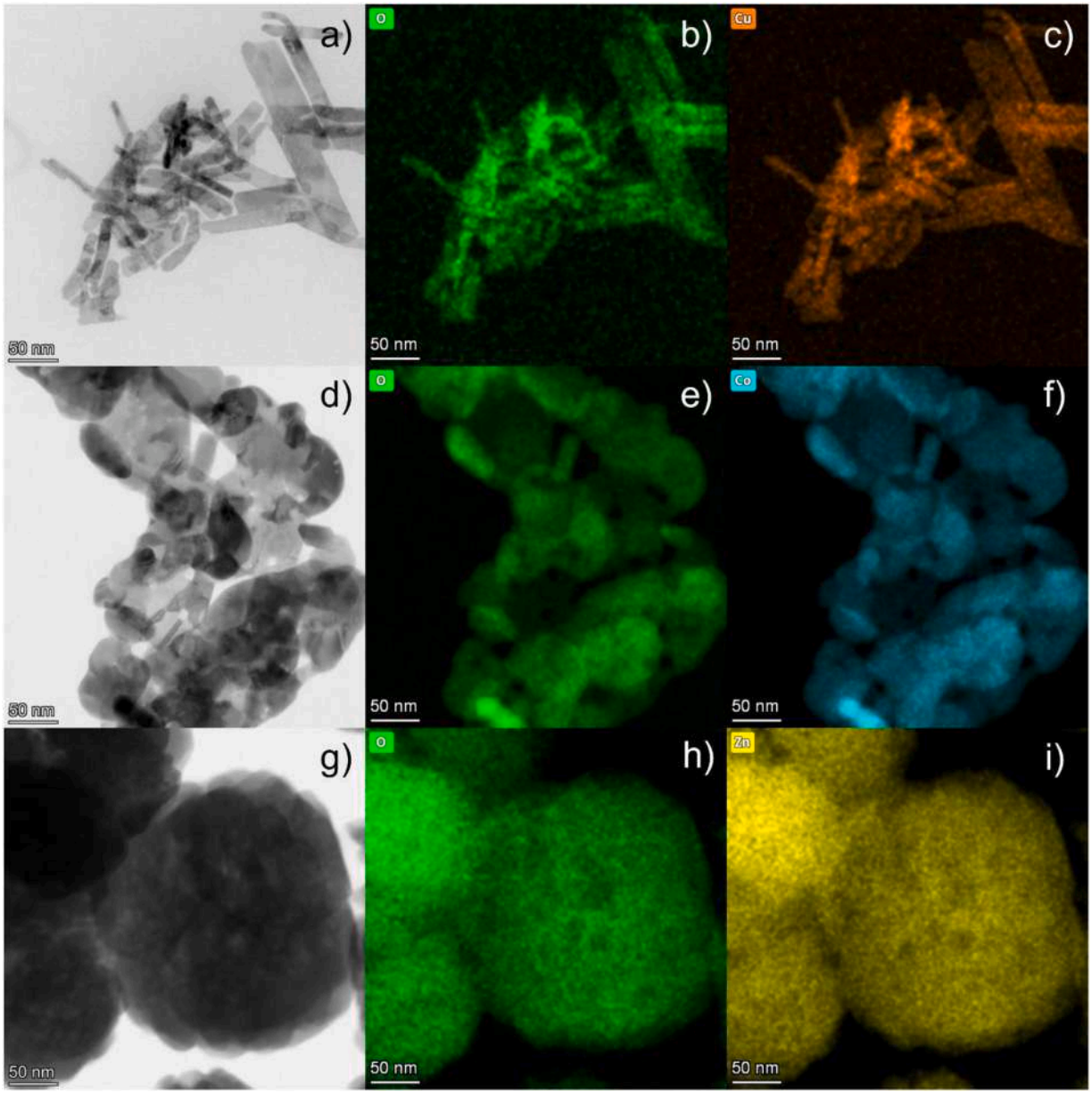

Fig. 5. STEM bright-field images (left) and EDX (middle, right) of (a-c) CuO, (d-f) Co_3O_4, and (g-i) ZnO nanoparticles. The first column (left) shows the corresponding STEM bright-field images, whereas the second and third columns display the spatial distribution of oxygen (middle) and the respective metal elements (Cu, Co, Zn) (right). All images are acquired at 270 KX magnifications.

are also high, increasing substantially and reaching 586.9 μmol h^{-1} cm^{-2} at −0.8 V. The corresponding NH_4^+ yield rate followed a similar trend, rising from 2.4 to 6.8 μmol h^{-1} cm^{-2} to 40.8 μmol h^{-1} cm^{-2} as the potential became more negative. (Fig. 7**c**)

These results clearly suggest that CuO primarily promotes the two-electron reduction of NO_3^- to NO_2^-, rather than the complete eight-electron pathway leading to NH_4^+.

Under the applied conditions (−0.8, −0.6 and −0.4 V vs. RHE, pH 6.3), CuO is thermodynamically unstable and tends to be reduced to metallic Cu [54]. This phase transformation is further supported by recent studies reporting the in-situ reconstruction of CuO into Cu/Cu_2O heterostructures under cathodic potentials. The high FE for NO_2^- observed in our experiments is therefore consistent with the intrinsic behavior of metallic Cu, which is known to facilitate the initial nitrate reduction to nitrite but to hinder subsequent hydrogenation steps due to its limited *H adsorption capability [55].

In our case, no synergistic enhancement typical of Cu/Cu_2O interfaces was observed. This can be attributed to the fibrous, needle-like morphology produced by the co-precipitation synthesis, which likely prevents the development of extended interfacial domains between Cu^0 and Cu^+ species that have been correlated with higher NH_3 selectivity in core–shell systems. Consequently, the catalytic performance of CuO after reduction is mainly governed by metallic Cu surfaces, favoring partial NO_3^- reduction to NO_2^- rather than the complete conversion to NH_4^+.

Among the individual oxides, Co_3O_4 displayed one of the most promising performances for NO_3RR, with the FEs for NH_4^+ increasing significantly with the applied potential, from 45.7 % at −0.4 V to 83.9 % at −0.6 V and 94.3 % at −0.8 V.(Fig. 7**a**) Similarly, the NH_4^+ yield rates rose markedly, from 15.3 to 149.5 μmol h^{-1} cm^{-2} across the same range, confirming both excellent selectivity and productivity, (Fig. 7**c**) while NO_2^- formation remained consistently low, with FEs around 1–2 % and corresponding yield rates below 6.5 μmol h^{-1} cm^{-2} at all potentials. (Fig. 7**b**) This reinforces the conclusion that Co_3O_4 efficiently drives the

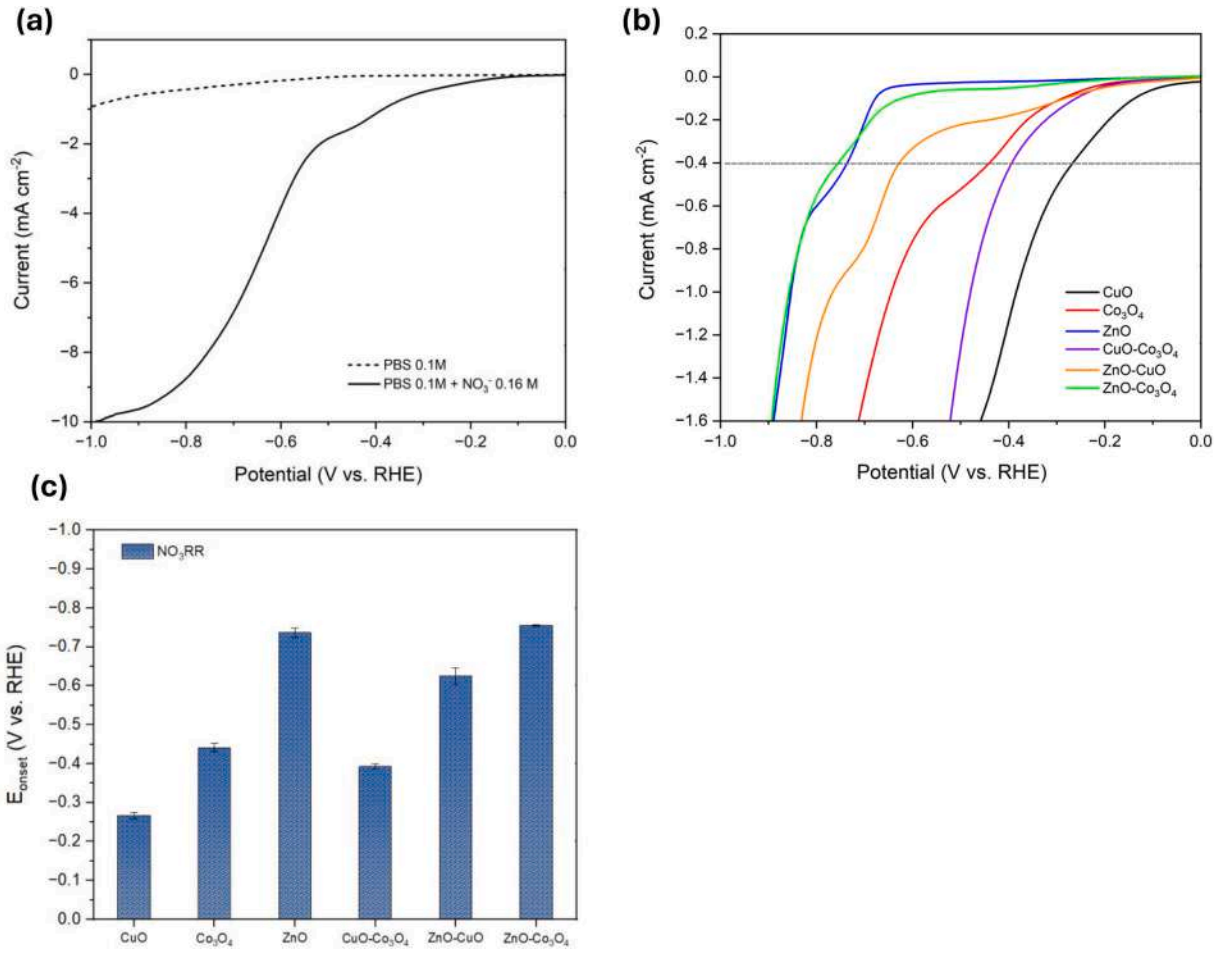

Fig. 6. (a) Representative LSV curves for the CuO EC in 0.1 M PBS (dotted line), and in 0.1 M PBS + 0.16 M NO_3^- (solid line). Complete LSV profiles for all tested electrocatalysts are provided in **Fig. S7**. (b) Magnified view of the LSV curves in 0.1 M PBS + 0.16 M NO_3^- for all ECs investigated. A horizontal dashed line at −0.4 mA cm^{-2} is included to visually indicate the potential threshold used in this work. The full-scale version of this plot is shown in **Fig. S7**. (c) Onset potentials for NO_3RR derived from the LSV data, defined as the potential at which a current density of −0.4 mA cm^{-2} is reached.

desired reduction of NO_3^- to NH_4^+, achieving high activity and selectivity, particularly at −0.8 V.

In Table 2, all the operating conditions and the results achieved by the studies used as comparisons involving Co-based electrocatalysts for NO_3RR are reported. The Co_3O_4 EC synthesized in this work demonstrates performance comparable and sometimes higher than the best-performing materials reported in the literature.

Finally, ZnO exhibited poor activity across all tested potentials, highlighting its limited suitability as a NO_3RR electrocatalyst. The FEs for NH_4^+ remained low, with values of 12.1 % at −0.4 V, 12.9 % at −0.6 V, and 15.4 % at −0.8 V (Fig. 7**a**) and the corresponding NH_4^+ yield rates were also minimal, ranging from 1.3 to 6.9 μmol h^{-1} cm^{-2}, indicating that only a small fraction of the electrons contributed to ammonium formation. (Fig. 7**c**) A sharp increase in NO_2^- production was observed between −0.6 V and −0.8 V vs. RHE, with the FE rising from 7.1 to 78.3 %, and the corresponding yield rate increasing from 2.17 to 141 μmol h^{-1} cm^{-2}. This behavior is further supported by the LSV analysis, which revealed an onset potential of −0.736 V vs. RHE, with the NO_3^-RR curve beginning to diverge significantly from the PBS background between −0.6 and −0.8 V. These results suggest that at −0.8 V, ZnO effectively activates the NO_3^- reduction, but, similarly to CuO, the reaction predominantly stops at the nitrite intermediate, rather than proceeding to full NH_4^+ formation.

In this potential–pH range, part of the ZnO phase may dissolve into the electrolyte as Zn^{2+} species rather than remaining fully stable in the solid state.[56] Moreover, the chronoamperometric curves recorded at −0.4 V and −0.6 V remained stable at approximately 1 and 4 mA cm^{-2}, respectively, suggesting that even in the case of dominant HER, the overall H_2 yield would be limited due to the low absolute current densities. This indicates that ZnO is not an efficient electrocatalyst for either NO_3RR or HER. Such behavior is consistent with previous reports showing that the intrinsically low electrical conductivity and wide band gap of ZnO hinder efficient charge transfer, resulting in generally poor electrocatalytic activity.[56]

After the examination of the individual transition metal oxides, our focus shifts to evaluating the performance of the corresponding binary mixtures of ECs, comparing how their combined properties influence NO_3RR efficiency and yield.

The binary mixture CuO–Co_3O_4 exhibited consistently high FEs toward NH_4^+ across all tested potentials, exceeding 70 % and reaching up to ~88 % at −0.8 V vs. RHE. (Fig. 7**a**) The corresponding NH_4^+ yield rates also followed a similar trend, peaking at ~149 μmol h^{-1} cm^{-2} at −0.8 V, values comparable to those obtained with pure Co_3O_4. These results indicate that the incorporation of CuO neither negatively impacts the NH_4^+ yield by Co_3O_4 nor provides a clear enhancement. (Fig. 7**c**) The formation of NO_2^- was significantly higher than with Co_3O_4 alone. At −0.8 V, the NO_2^- yield rate increased from ~6.5 μmol h^{-1} cm^{-2} (Co_3O_4) to ~80.8 μmol h^{-1} cm^{-2} in the binary mixture CuO–Co_3O_4, suggesting that CuO contributes to the initial NO_3^--to-NO_2^- conversion steps. (Fig. 7**b**) However, this effect does not translate into improved NH_4^+ yield, implying the absence of a true tandem mechanism. Instead, the two oxides appear to operate in parallel, with Co_3O_4 remaining the main

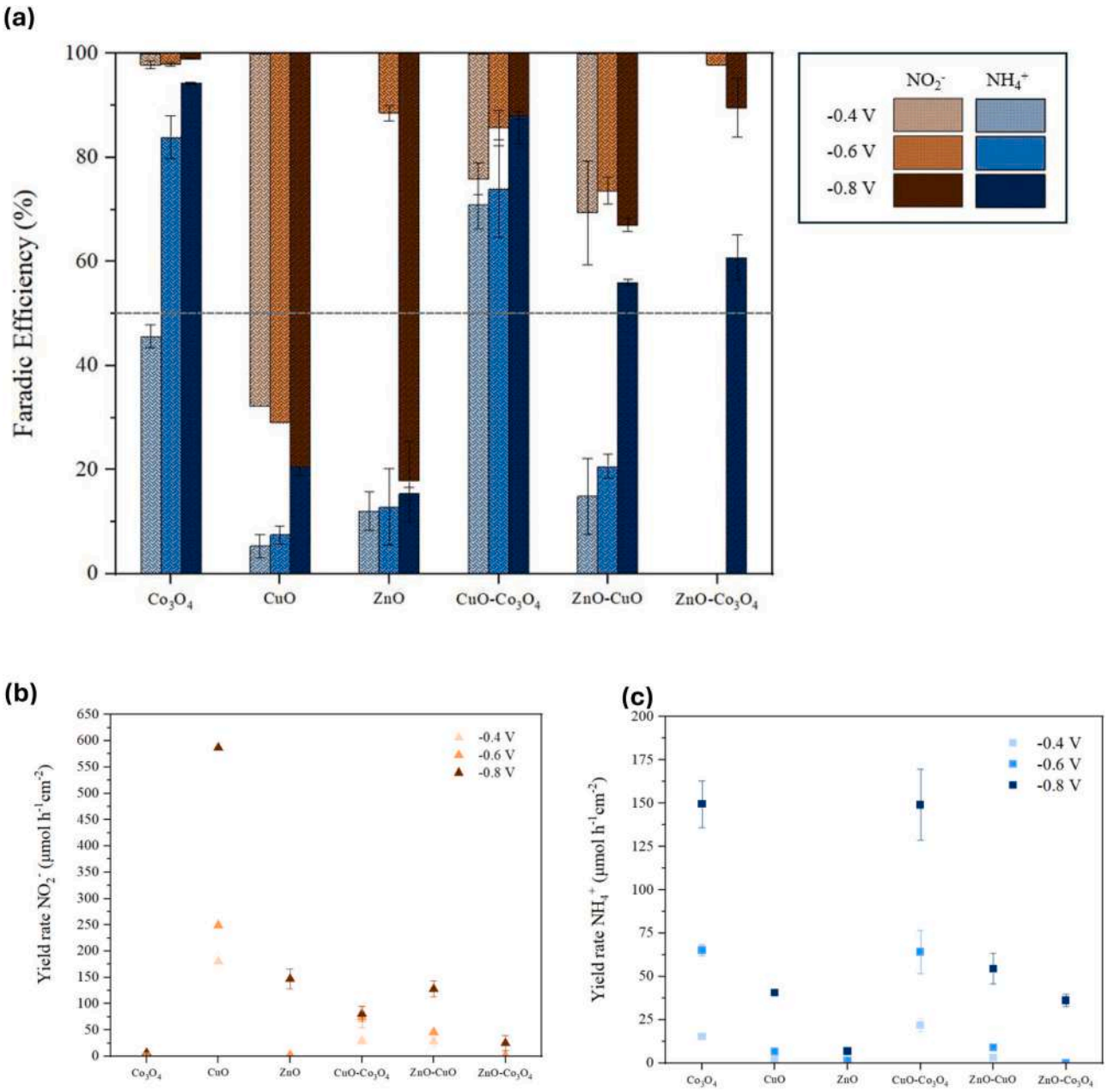

Fig. 7. Gap analysis plot (GAP) for the electrochemical NO_3RR for all ECs in 0.1 M PBS+0.16 M NO_3^- for 1 h. a) Faradaic efficiency for NO_2^- (orange; top-down) and NH_4^+ (blue; bottom-up) at −0.4 V, −0.6 V and −0.8 V vs. RHE. A horizontal line is set at 50 % FE to guide the eye. The bottom section of the figure shows the corresponding yield rate (μmol h^{-1} cm^{-2}) for b) NO_2^- (orange, triangle) and c) NH_4^+ (blue, square) as a function of the applied potentials. A simplified plot is reported in **Fig. S12-S13,** whereas the data are presented in **Table S1-S2.**

contributor to the full reduction of NO_3^- to NH_4^+.

Instead, the binary mixture ZnO–Co_3O_4 exhibited negligible activity at −0.4 V and −0.6 V, with no detectable formation of either NO_2^- or NH_4^+. (Fig. 7**a**) This behavior aligns with the LSV curves, which show a delayed onset potential and a noticeable divergence from the PBS background only between −0.6 V and −0.8 V vs. RHE. At −0.8 V, product formation becomes evident, with a FE of 60.7 % and a yield rate of 36.2 μmol h^{-1} cm^{-2} for NH_4^+. (Fig. 7**c**) These results indicate a shift toward a reduction pathway favoring NH_4^+ over NO_2^-, contrasting with the behavior of pure ZnO, which at the same potential primarily produces NO_2^-. (Fig. 7**b**) However, the FE and productivity are significantly lower than that of the pure Co_3O_4 and this suggests that ZnO may alter surface properties or active site accessibility. Overall, the binary mixture ZnO–Co_3O_4 shows no advantage over single ECs and does not exhibit meaningful synergy between its components.

Among the binary mixtures, ZnO–CuO exhibited the most complex behavior in terms of product selectivity and activity. At −0.4 V and −0.6 V, both the FE and the yield rate for NH_4^+ remained modest (14.9–20.7 % FE and <9 μmol h^{-1} cm^{-2}), whereas at −0.8 V the NH_4^+ FE increased significantly to 56.0 %, with a corresponding yield rate of 54.5 μmol h^{-1} cm^{-2}, surpassing both pure CuO and ZnO. This unexpected enhancement in NH_4^+ selectivity at −0.8 V is particularly notable because, when tested separately, both ZnO and CuO primarily facilitated the partial reduction of NO_3^- to NO_2^-. The synergistic effect observed in the ZnO–CuO system may be due to a modification either in the surface chemistry or in the electronic structure upon mixing, which could promote further hydrogenation steps otherwise disfavored in the single ECs. The binary mixture ZnO–CuO appears to partially overcome the limitations of the individual components, enabling a more balanced selectivity between NO_2^- and NH_4^+ and improved NH_4^+ productivity at high overpotentials.

Table 2
Comparison of the catalytic performance of different Co-based ECs in NO_3RR in previous work.

Electrocatalyst	Overpotential (V vs. RHE)	Electrolyte	FE (%)	NH_3 Yield Rate (mmol h^{-1} cm^{-2})	Ref
Co_3O_4 NPs	−0.8	PBS 0.1 *M* + 0.16 M NO_3^-	94.3	0.16	This Work
Co_3O_4@TiO_2/TP	−0.7	0.1 NaOH + 0.1 NO_3^-	93.1	0.7	[29]
CoP NRs	−0.5	0.5 Na_2SO_4 + 0.05 NO_3^-	97.1	0.2	[32]
Co-P/TP	−0.3	0.2 Na_2SO_4 + 0.2 NO_3^-	93.6	0.02	[33]
$ZnCo_2O_4$	−0.4	0.1 KOH + 0.1 NO_3^-	95.4	0.03	[34]
VCo-Co_3O_4/CC	−0.4	0.1 NaOH + 0.1 NO_3^-	97.2	0.38	[40]
($Cu_{0.6}Co_{0.4}$) Co_2O_4	−0.45	1 KOH + 0.1 NO_3^-	96.5	1.09	[35]
$Mn_2Co_3O_4$	−0.6	0.1 PBS + 0.1 NO_3^-	98.6	0.3	[43]
$CoMn_2O_4$/NC	−0.7	0.1 Na_2SO_4 + 0.1 NO_3^-	92.4	0.058	[36]
Co_2NiO_4	−1.0	0.5 K_2SO_4 + 0.1 NO_3^-	94.9	1.18	[37]
Pd-CoO/NF	−1.36	0.5 K_2SO_4 + 200 ppm NO_3^-	88.6	0.2044	[38]
Co_3O_4/MWCNTs	−0.16	0.1 KOH + 0.1 NO_3^-	84.72	0.237	[41]
Co_3O_4/Co-h	−0.8	0.1 M Na_2SO_4 + 1 mg mL^{-1} NO_3^-	88.7	0.26	[42]
$La_{0.6}Sr_{0.4}CoO_3$	−0.78	0.5 M Na_2SO_4 + 0.1 M NO_3^-	85.6	0.427	[39]

Nevertheless, the mechanism underlying this apparent synergy remains unclear.

Overall, the binary mixture investigated displayed non-linear and often unpredictable behaviors, with trends in selectivity and activity that were not simply the sum or average of the individual components.

This outcome can be attributed to the fact that the mixed electrocatalysts were prepared by simple mechanical blending of the individual oxides, which does not ensure intimate interfacial contact or the formation of coherent heterojunctions. Consequently, the electronic coupling between the two phases is weak, limiting interfacial charge transfer and preventing the synergistic effects typically observed in well-engineered mixed systems.

Since Co_3O_4 exhibited the highest NO_3RR activity among the investigated ECs, its operational stability was further evaluated through ten consecutive chronoamperometric cycles at −0.8 V vs. RHE. Each cycle lasted 1 h, after which the electrolyte was replaced with a fresh solution before the subsequent run. After every cycle, the concentrations of NH_4^+ and NO_2^- were quantified to calculate the corresponding FEs and yield rates.

Under these conditions, Co_3O_4 demonstrated remarkable stability, consistently maintaining a FE for NH_4^+ above 90 % throughout all cycles, with only negligible NO_2^- formation (**Fig. S14**).

Before and after the tenth cycle, the catalyst was characterized by XRD and XPS to verify the preservation of the crystalline phase and to monitor possible variations in the surface oxidation states.

Figure **S15** shows the XRD patterns of the carbon paper and the Co_3O_4 deposited on the carbon paper before and after 10 cycles. The diffractogram displays the characteristic peaks of Co_3O_4 (marked in red) and the carbon support (in grey). For the carbon paper the XRD pattern shows the key peaks at 2θ = 26.5° (002), 44.5° (101), 54.7° (004), and 77.4° (110), which are typical for carbon with hexagonal structure (card number 03–065–6212, ICDD), while for Co_3O_4, the XRD pattern exhibits the main reflections at 2θ = 31.3° (220), 36.8° (311), 38.5° (222), 44.8° (400), 55.6° (422), 59.3° (511), 65.2° (440), 69.7° (531) and 77.3° (533), which are in good agreement with the standard reference pattern of the spinel Co_3O_4 phase (card number 00–043–1003, ICDD).

A comparison between the samples before and after cycling reveals that the positions of the Co_3O_4 peaks remain unchanged, with no evidence of peak shifting or broadening. This indicates that the crystalline structure of Co_3O_4 is well preserved and that no phase transformation or significant degradation of the structure occurs during the electrocatalytic process. The results confirm the excellent structural stability of our material when supported on carbon paper, even after repeated redox cycling.

The surface chemical composition of the Co_3O_4 deposited on the carbon paper before and after electrolysis was further examined by XPS of the Co $2p_{3/2}$ region.

The spectra were deconvoluted into two main components centered at 780.6 eV and 779.5 eV, corresponding to Co^{2+} and Co^{3+} species, respectively. (**Fig S16**)

Before electrolysis, the Co^{2+} fraction was 78 %, while after the tenth cycle, this ratio slightly decreased to 73 %, with a corresponding increase in the Co^{3+} contribution from 22 % to 27 %.

The high proportion of Co^{2+} species observed on the surface is consistent with the elevated FE achieved, as NO_3RR is reported to preferentially occur on Co^{2+} rather than Co^{3+} sites. Such a minor variation suggests limited surface re-oxidation while preserving the overall Co^{2+}-rich character of the electrocatalyst.

These results confirm that the Co_3O_4 surface maintains its chemical stability during prolonged operation, consistent with the nearly constant FE observed over repeated cycles and with the absence of detectable structural changes in the XRD patterns discussed below.

To better understand Co_3O_4 electrocatalytic properties and the role of nitrate concentration, a series of 1-h potential holds were performed at −0.40 V, −0.60 V, and −0.80 V vs. RHE in 0.04, 0.08, and 0.12 M NO_3^-, in addition to the 0.16 M previously discussed (Fig. 8).

The corresponding current–time profiles for each concentration of NO_3^- are shown in **Fig. S17-S18.**

The results revealed a clear dependence of the NH_4^+ yield rate on the nitrate concentration, particularly at more negative potentials. At −0.8 V, increasing the nitrate concentration led to a nearly linear enhancement in NH_4^+ production, reaching a maximum yield rate of 149.5 μmol h^{-1} cm^{-2} at 0.16 M. Similarly, at −0.6 V, the yield rate rose from 14.6 to 65.1 μmol h^{-1} cm^{-2} across the tested concentrations. At −0.4 V, however, the yield rates were generally lower and exhibited no clear concentration-dependent trend, suggesting that mass transport limitations or low overpotential might hinder the reaction under these conditions.

In terms of FE, the highest values for NH_4^+ were obtained at −0.8 V across all concentrations, exceeding 90 %, except at 0.04 M, where it dropped to 82.7 %. A similar behavior was noted at −0.6 V, with FE values stable around 82 % for 0.08, 0.12, and 0.16 M, but significantly lower at 0.04 M (66.5 %), likely reflecting kinetic limitations at low nitrate availability.

Finally, at −0.4 V, lower FE values and greater variability are observed across different concentrations, with FEs ranging from approximately 45 % to over 80 %. Regarding NO_2^-, across all potentials and concentrations, Co_3O_4 showed extremely low FE toward NO_2^-, generally below 3 %, with yield rates rarely exceeding 7.5 μmol h^{-1} cm^{-2} even at higher concentrations. This confirms that the EC favors full reduction to ammonium and effectively suppresses the accumulation of partially reduced intermediates.

In summary, increasing the nitrate concentration enhances the NH_4^+ yield rate on Co_3O_4, especially under highly cathodic conditions, while preserving high FEs and suppressing NO_2^- formation.

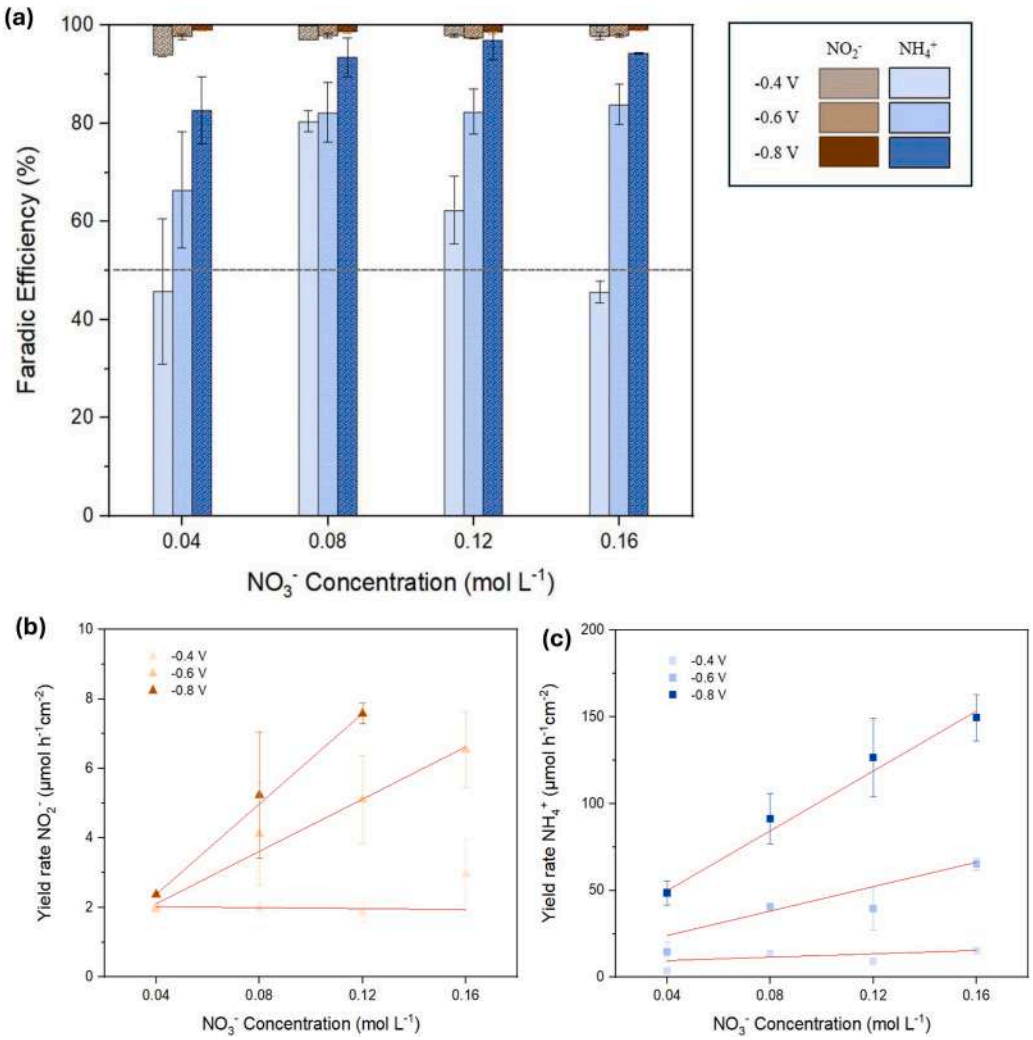

Fig. 8. GAP for the electrochemical NO_3RR for 1 h for all NO_3^- concentrations: 0.04, 0.08, 0.12 and 0.16 M a) FE for NO_2^- (orange; top-down) and NH_4^+ (blue; bottom-up) at −0.4 V, −0.6 V and −0.8 V vs. RHE. A horizontal line is set at 50 % FE to guide the eye. The bottom section of the figure shows the corresponding yield rate (μmol h^{-1} cm^{-2}) for b) NO_2^- (orange, triangle) and c) NH_4^+ (blue, square) as a function of the applied potentials. A linear fit has been applied to the NH_4^+ and NO_2^- yield rate. A simplified plot is reported in **Fig.S19–20,** while the data are presented in **Table S4-S5.**

4. Conclusion

In this work, we systematically investigated and compared the electrocatalytic performance of three metal oxide ECs (namely, CuO, ZnO, and Co_3O_4) for the NO_3RR. All materials were synthesized following a co-precipitation route in an alkaline environment. Despite being obtained following the same synthesis protocol and exhibiting comparable nanometric dimensions, the three oxides showed completely distinct morphologies: CuO formed fibrous needle-like structures, Co_3O_4 displayed a plate-like morphology, and ZnO consisted of cauliflower-like agglomerated particles.

Among the tested oxides, Co_3O_4 emerged as the most promising EC, achieving a FE of 94.3 % and a yield rate of 149.5 μmol h^{-1} cm^{-2} for NH_4^+ at −0.8 V vs RHE. Nitrite formation was consistently low, with FEs below 2 % and yield rates under 6.5 μmol h^{-1} cm^{-2} across all potentials, confirming the high selectivity of Co_3O_4 toward the complete eight-electron reduction pathway.

Co_3O_4 also demonstrated remarkable durability, maintaining a Faradaic efficiency for NH_4^+ above 90 % over ten consecutive 1-h chronoamperometric cycles at −0.8 V vs. RHE, with negligible NO_2^- formation and no detectable structural changes in the XRD patterns. XPS analysis further confirmed the preservation of the surface composition, showing only minor variations in the Co^{2+}/Co^{3+} ratio after cycling. Furthermore, the high proportion of Co^{2+} species observed on the surface (78 %) is consistent with the elevated FE achieved, as NO_3RR is reported to preferentially occur on Co^{2+} rather than Co^{3+} sites.

Additionally, we evaluated the impact of nitrate concentration on the performance of Co_3O_4. The NH_4^+ yield rate increased with rising NO_3^- concentration, particularly under more negative potentials, while maintaining high faradaic efficiencies and minimal NO_2^- formation.

CuO, in contrast, exhibited excellent specificity for NO_3^- reduction to NH_3, as demonstrated by LSV measurements, with early activation of the NO_3RR and effective suppression of the competing HER. However, it showed limited ability to drive the complete eight-electron reduction pathway, with a FE for NH_4^+ of only 20.8 % at −0.8 V vs RHE.

Conversely, CuO consistently favored NO_2^- formation, with FEs exceeding 80 % and yield rates around 550 μmol h^{-1} cm^{-2} at the most negative potential tested. These results clearly indicate that CuO primarily promotes the two-electron reduction of NO_3^- to NO_2^-, while the hydrogenation steps required for full conversion to NH_4^+ remain largely inactive.

Lastly, ZnO exhibited the weakest performance among the tested ECs. The LSV curves revealed nearly overlapping responses in PBS and nitrate-containing electrolytes, accompanied by a delayed onset potential, indicating poor activation toward NO_3^-RR. Some catalytic activity was observed only at highly negative potentials, where the FE for NO_2^-

reached 78.3 %, with a corresponding yield rate of 141 μmol h^{-1} cm^{-2}. This behavior resembles that of CuO, although with a yield rate approximately four times lower.

Finally, the binary mixtures investigated displayed non-linear and often unpredictable behaviors, with trends in selectivity and activity that were not simply the sum or average of the individual components. This outcome can be attributed to the simple mechanical blending of the individual oxides, which results in weak electronic coupling between the two phases and limits interfacial charge transfer.

Declaration of competing interest

The authors declare that they have no known competing financial interests or personal relationships that could have appeared to influence the work reported in this paper.

Acknowledgements

S.L., M.M. and C.S. would like to acknowledge the European Union −NextGeneration EU from the Italian Ministry of Environment and Energy Security POR H2 AdP MMES/ENEA with involvement of CNR and RSE, PNRR - Mission 2, Component 2, Investment 3.5 “Ricerca e sviluppo sull’idrogeno” under the ENEA − UNIMIB agreement (Procedure 1.1.3 PNRR POR H_2).

Supplementary materials

Supplementary material associated with this article can be found, in the online version, at doi:10.1016/j.electacta.2025.147870.

References

[1] Z.J. Schiffer, K. Manthiram, Electrification and decarbonization of the chemical industry, Joule 1 (2017) 10–14, https://doi.org/10.1016/j.joule.2017.07.008. Preprint at.
[2] Iea, Technology Roadmap Energy and GHG Reductions in the Chemical Industry Via Catalytic Processes, 2013.
[3] M. Nazemi, S.R. Panikkanvalappil, M.A. El-Sayed, Enhancing the rate of electrochemical nitrogen reduction reaction for ammonia synthesis under ambient conditions using hollow gold nanocages, Nano Energy 49 (2018) 316–323.
[4] M. Muhyuddin, et al., Electrochemical urea production using carbon dioxide and nitrate: state of the art and perspectives, Energy Environ. Sci. 17 (2024) 3739–3752, https://doi.org/10.1039/d4ee00561a. Preprint at.
[5] M.H. Hasan, et al., A comprehensive review on the recent development of ammonia as a renewable energy carrier, Energies 14 (2021), https://doi.org/10.3390/en14133732. Preprint at.
[6] G.J. Leigh, Haber-Bosch and other industrial processes, in: B.E. Smith, R. L. Richards, W.E. Newton (Eds.), Catalysts For Nitrogen Fixation: Nitrogenases, Relevant Chemical Models and Commercial Processes, Springer Netherlands, Dordrecht, 2004, pp. 33–54, https://doi.org/10.1007/978-1-4020-3611-8_2.
[7] Y. Ren, et al., Strategies to suppress hydrogen evolution for highly selective electrocatalytic nitrogen reduction: challenges and perspectives, Energy Environ. Sci. 14 (2021) 1176–1193, https://doi.org/10.1039/d0ee03596c. Preprint at.
[8] S.L. Foster, et al., Catalysts for nitrogen reduction to ammonia, Nat. Catal. 1 (2018) 490–500.
[9] H. Iriawan, et al., Methods for nitrogen activation by reduction and oxidation, Nat. Rev. Methods Primers. 1 (2021) 56.
[10] X. Cui, C. Tang, Q. Zhang, A review of electrocatalytic reduction of dinitrogen to ammonia under ambient conditions, Adv. Energy Mater. 8 (2018), https://doi.org/10.1002/aenm.201800369. Preprint at.
[11] P.H. van Langevelde, I. Katsounaros, M.T.M. Koper, Electrocatalytic nitrate reduction for sustainable Ammonia production, Joule 5 (2021) 290–294.
[12] J. Long, et al., Direct electrochemical ammonia synthesis from nitric oxide, Angew. Chem. Int. Ed. 59 (2020) 9711–9718.
[13] Y. Wang, C. Wang, M. Li, Y. Yu, B. Zhang, Nitrate electroreduction: mechanism insight,: in situ characterization, performance evaluation, and challenges, Chem. Soc. Rev. 50 (2021) 6720–6733, https://doi.org/10.1039/d1cs00116g. Preprint at.
[14] Y. Zeng, C. Priest, G. Wang, G. Wu, Restoring the nitrogen cycle by electrochemical reduction of nitrate: progress and prospects, Small. Methods 4 (2020), https://doi.org/10.1002/smtd.202000672. Preprint at.
[15] P. Wang, et al., Efficient hydrogen generation and total nitrogen removal for urine treatment in a neutral solution based on a self-driving nano photoelectrocatalytic system, Nanomaterials 11 (2021).
[16] *Nitrate and Nitrite in Drinking-Water Background Document for Development of WHO Guidelines for Drinking-Water Quality*. http://www.who.int/publications/guidelines/.
[17] K.M. Moloantoa, Z.P. Khetsha, E. van Heerden, J.C. Castillo, E.D. Cason, Nitrate water contamination from industrial activities and complete denitrification as a remediation option, Water 14 (2022), https://doi.org/10.3390/w14050799. Preprint at.
[18] P. Cyplik, et al., Biological denitrification of high nitrate processing wastewaters from explosives production plant, Water. Air. Soil. Pollut. 223 (2012) 1791–1800.
[19] K. Velusamy, et al., Advanced techniques to remove phosphates and nitrates from waters: a review, Env. Chem. Lett. 19 (2021) 3165–3180, https://doi.org/10.1007/s10311-021-01239-2. Preprint at.
[20] T.K.M. Prashantha Kumar, T.R. Mandlimath, P. Sangeetha, S.K. Revathi, S.K. Ashok Kumar, Nanoscale materials as sorbents for nitrate and phosphate removal from water, Env. Chem. Lett. 16 (2018) 389–400, https://doi.org/10.1007/s10311-017-0682-7. Preprint at.
[21] L. Barrera, R. Bala Chandran, Harnessing photoelectrochemistry for wastewater nitrate treatment coupled with resource recovery, ACS. Sustain. Chem. Eng. 9 (2021) 3688–3701.
[22] S. Kotopoulou, A. Zampelas, E. Magriplis, Dietary nitrate and nitrite and human health: a narrative review by intake source, Nutr. Rev. 80 (2022) 762–773, https://doi.org/10.1093/nutrit/nuab113. Preprint at.
[23] G.M. Taylor, et al., Severe methemoglobinemia secondary to isobutyl nitrite toxicity: the case of the ‘Gold Rush’, Oxf. Med. Case Rep. 2021 (2021) 55–58.
[24] C. Smith, A.K. Hill, L. Torrente-Murciano, Current and future role of Haber-Bosch ammonia in a carbon-free energy landscape, Energy Env. Sci. 13 (2020) 331–344.
[25] T. Hu, C. Wang, M. Wang, C.M. Li, C. Guo, Theoretical insights into superior nitrate reduction to ammonia performance of copper catalysts, ACS. Catal. 11 (2021) 14417–14427.
[26] M. Karamad, T.J. Goncalves, S. Jimenez-Villegas, I.D. Gates, S. Siahrostami, Why copper catalyzes electrochemical reduction of nitrate to ammonia, Faraday Discuss. 243 (2022) 502–519.
[27] J.Y. Fang, J.L. Fan, S.B. Liu, S.P. Sun, Y.Y. Lou, Copper-based electrocatalysts for nitrate reduction to Ammonia, Materials 16 (2023), https://doi.org/10.3390/ma16114000. Preprint at.
[28] S. Lombardi, et al., Design strategies to enhance copper electrocatalytic performance for nitrate-to-ammonia electroreduction, ChemElectroChem. (2025), https://doi.org/10.1002/celc.202400482. Preprint at.
[29] X. Fan, et al., Unveiling selective nitrate reduction to ammonia with Co3O4 nanosheets/TiO2 nanobelt heterostructure catalyst, J. Colloid. Interface Sci. 630 (2023) 714–720.
[30] T. Ren, et al., Concave-convex surface oxide layers over copper nanowires boost electrochemical nitrate-to-ammonia conversion, Chem. Eng. J. 426 (2021).
[31] X. Meng, et al., Recent progress in cobalt-based electrocatalysts for efficient electrochemical nitrate reduction reaction, Adv. Funct. Mater. 35 (2025), https://doi.org/10.1002/adfm.202418492. Preprint at.
[32] Q.L. Hong, et al., Cobalt phosphide nanorings towards efficient electrocatalytic nitrate reduction to ammonia, Chem. Commun. 57 (2021) 11621–11624.
[33] Z. Li, et al., High-efficiency nitrate electroreduction to ammonia on electrodeposited cobalt-phosphorus alloy film, Chem. Commun. 57 (2021) 9720–9723.
[34] P. Huang, et al., 3D Flower-like zinc cobaltite for electrocatalytic reduction of nitrate to ammonia under ambient conditions, ChemSusChem. 15 (2022).
[35] Q. Hu, et al., Designing efficient nitrate reduction electrocatalysts by identifying and optimizing active sites of Co-based spinels, J. Am. Chem. Soc. 146 (2024) 2967–2976.
[36] Z. Niu, S. Fan, X. Li, J. Duan, A. Chen, Interfacial engineering of CoMn2O4/NC induced electronic delocalization boosts electrocatalytic nitrogen oxyanions reduction to ammonia, Appl. Catal. B 322 (2023).
[37] L. Qiao, et al., Nickel-facilitated in-situ surface reconstruction on spinel Co3O4 for enhanced electrochemical nitrate reduction to ammonia, Appl. Catal. B 340 (2024).
[38] M. Liu, et al., Electroreduction of nitrate to ammonia on palladium-cobalt-oxygen nanowire arrays, ACS. Appl. Mater. Interfaces. 14 (2022) 13169–13176.
[39] J. Zhao, D. Cao, J. Yao, K. Zhu, H. Zhao, Effects of crystal phase in cobalt-based perovskite for electro- reduction of nitrate to ammonia, Appl. Surf. Sci. 685 (2025).
[40] Z. Deng, et al., High-efficiency electrochemical nitrate reduction to ammonia on a Co3O4Nanoarray catalyst with cobalt vacancies, ACS. Appl. Mater. Interfaces. 14 (2022) 46595–46602.
[41] M. Ye, et al., Enhanced electrocatalytic nitrate reduction to ammonia using functionalized multi-walled carbon nanotube-supported cobalt catalyst, Nanomaterials 14 (2024).
[42] F. Zhao, G. Hai, X. Li, Z. Jiang, H. Wang, Enhanced electrocatalytic nitrate reduction to ammonia on cobalt oxide nanosheets via multiscale defect modulation, Chem. Eng. J. 461 (2023).
[43] D. Liu, et al., Electrocatalytic reduction of nitrate to ammonia on low-cost manganese-incorporated Co3O4 nanotubes, Appl. Catal. B 324 (2023).
[44] Y. Sun, et al., Electroreduction of nitrate into ammonia on Co3O4: mechanistic insights into Co2+-promoted NO3RR performance, Chem. Eng. J. 512 (2025).
[45] Z. Pan, et al., Synthesis of a Ga-doped La5Ti2Cu0.9Ag0.1O7S5 photocatalyst by thermal sulfidation for hydrogen evolution under visible light, J. Catal. 399 (2021) 230–236.
[46] K.B. Tom, et al., Solution-based, template-assisted realization of large-scale graphitic ZnO, ACS. Nano 12 (2018) 7554–7561.
[47] J. Lee, D.C. Sorescu, X. Deng, Tunable lattice constant and band gap of single- and few-layer ZnO, J. Phys. Chem. Lett. 7 (2016) 1335–1340, https://doi.org/10.1021/acs.jpclett.6b00432. Preprint at.
[48] A. Feng, et al., ZnO nanowire arrays decorated with Cu nanoparticles for high-efficiency nitrate to ammonia conversion, ACS. Catal. 14 (2024) 5911–5923.

[49] T.S. Bui, et al., Enhanced nitrate-to-ammonia activity on Fe/ZnO nanoparticles via tuning intermediate adsorption in alkaline electrolyte, Adv. Funct. Mater. 34 (2024).
[50] W. Fu, et al., Electrocatalytic conversion of nitrate to ammonia on the oxygen vacancy engineering of zinc oxide for nitrogen recovery from nitrate-polluted surface water, Env. Res. 264 (2025).
[51] M.C. Biesinger, L.W.M. Lau, A.R. Gerson, R. Smart, Resolving surface chemical states in XPS analysis of first row transition metals, oxides and hydroxides: *sc*, Ti, V, Cu and Zn, Appl. Surf. Sci. 257 (2010) 887–898.
[52] M.C. Biesinger, et al., Resolving surface chemical states in XPS analysis of first row transition metals, oxides and hydroxides: Cr, Mn, Fe, Co and Ni, Appl. Surf. Sci. 257 (2011) 2717–2730.
[53] E. Murphy, et al., Elucidating electrochemical nitrate and nitrite reduction over atomically-dispersed transition metal sites, Nat. Commun. 14 (2023).
[54] W. Wen, P. Yan, W. Sun, Y. Zhou, X.Y. Yu, Metastable phase Cu with optimized local electronic State for efficient electrocatalytic production of ammonia from nitrate, Adv. Funct. Mater. 33 (2023).
[55] M. Nie, et al., Study on electrocatalytic property of ZnO and Ag/ZnO, Mater. Lett. 271 (2020).